Engineering Applications of Artificial Intelligence 160 (2025) 111866

Contents lists available at ScienceDirect

Engineering Applications of Artificial Intelligence

journal homepage: www.elsevier.com/locate/engappai

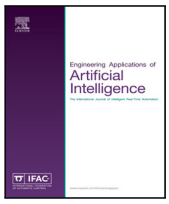

Research paper

Defect detection and data generation of shunt between three layers of resistance spot welding based on deep convolutional generative adversarial network and conditional variational autoencoder

Haofeng Deng [a], Xiangdong Gao [a,b,*], Dongfang Zhang [a], Wuqi Lu [a], Pengyu Gao [a], Yanxi Zhang [a]

[a] Guangdong Provincial Welding Engineering Technology Research Center, Guangdong University of Technology, Guangzhou, 510006, China
[b] Guangzhou Zhengtian Technology Company, Guangzhou, 510006, China

ARTICLE INFO

Keywords:
Resistance spot welding
Three layers
Interplate shunt effect
Data generation
Deep convolutional generative adversarial network
Conditional variational autoencoder

ABSTRACT

Resistance spot welding (RSW), as a widely used joining technology in the automotive industry, especially in the welding process of three-layer plates, makes it difficult to concentrate the welding current to the target area due to the inter-plate shunt effect, which reduces the quality of the formation of the molten nucleus and increases the incidence of weld defects. To cope with this problem, this paper proposes a defect generation and classification method based on a Deep Convolutional Generative Adversarial Network-Conditional Variational Autoencoder (DCGAN-CVAE), which is used to generate synthetic defect data and augment limited real-world samples. The optimal welding process parameters are found through one-way experiments on welding current, welding time, and electrode pressure combined with Analysis of Variance and response surface analysis. Based on the optimal parameters, we conduct inter-plate shunt experiments, collect dynamic resistance signals, generate and expand defect samples through the DCGAN-CVAE generation model, and finally verify the classification of the generated samples using the Bidirectional Long Short-Term Memory network-One Dimensional Convolutional Neural Network (BiLSTM-1DCNN) classifier. Experimental results show that the generated data effectively improves the accuracy of defect detection, and the generated data have high similarity with the real data, which can provide data support for quality control in actual production.

1. Introduction

Resistance spot welding (RSW) is widely used in automotive manufacturing due to its simplicity, speed, and cost-effectiveness (Chen et al., 2022a; Xiao et al., 2023). In specific applications, particularly when welding steel plates of varying thicknesses and strengths, three-layer plate RSW is becoming increasingly prevalent (Pouranvari and Marashi, 2012). This technique involves the simultaneous joining of three overlapping metal sheets, typically applied in key structural areas such as car body side frames and floor reinforcements to improve overall stiffness and reduce process steps. However, this method presents greater complexity than two-layer welding, as the additional layer and varying thickness at the contact surfaces complicate the process. The middle layer, being less exposed to the electrodes, experiences uneven heat generation and dissipation, leading to irregular molten nugget formation and varied weld morphology at the interfaces, complicating analysis (Shen et al., 2011).

A common defect in multilayer resistance spot welding (RSW) is the interplate shunt effect (Li et al., 2013), where part of the welding current bypasses the intended weld zone and instead flows through alternative low resistance paths between the outer plates. This unintended current diversion reduces the effective current passing through the target interface, particularly the middle layer, resulting in insufficient heat generation at the weld joint. The welding parameters, material properties, and surface conditions influence the severity of the shunt effect. As a consequence, the formation of a proper molten core is hindered, and the resulting weld may suffer from various quality issues such as spatter, surface burns, excessive indentation, or internal defects like shrinkage holes, cracks, and irregular nugget morphology (Xia et al., 2021).

When these defects are within acceptable limits, key quality indicators like molten core diameter, surface indentation depth, and mechanical properties become critical for assessing mechanical strength.

* Corresponding author at: Guangdong Provincial Welding Engineering Technology Research Center, Guangdong University of Technology, Guangzhou, 510006, China.
E-mail addresses: 1112301044@mail2.gdut.edu.cn (H. Deng), gaoxd@gdut.edu.cn (X. Gao), 1084511763@qq.com (D. Zhang), 2324270550@qq.com (W. Lu), perrypgao@gmail.com (P. Gao), yanxizhang@gdut.edu.cn (Y. Zhang).

https://doi.org/10.1016/j.engappai.2025.111866
Received 27 December 2024; Received in revised form 14 June 2025; Accepted 22 July 2025
Available online 16 August 2025

These indicators are significantly influenced by spot welding parameters, which are essential for ensuring surface quality and the overall performance of welded components (Dai et al., 2022). Nielsen et al. (2011) noted that low-carbon Multilayer steel joints have a more complex internal structure than two-layer plates, leading to uneven current distribution in the nugget region and reduced heat dissipation efficiency. This results in increased defects such as interplate shunting and spattering in three-layer welding. Pouranvari and Marashi (2011) found that nugget formation in thicker three-layer low-carbon steel plates takes longer, although the growth rate is faster due to increased body resistance. In welding 0.8/1.9/1.9 mm DP600 plates, optimal tensile strength requires ensuring a minimum nugget size, highlighting the challenges of achieving high-quality welds in multilayer configurations. This underscores the need for multi-factor, multi-objective analyses to optimize joint performance. Given the complexity of multilayer welding, statistical methods like Response Surface Methodology (RSM) are frequently employed for parameter optimization (Chen et al., 2022b). RSM has been widely applied in welding optimization. For instance, MohammadiSefat et al. (2021) utilized thermal modeling to investigate how parameters such as rotational speed and shoulder diameter affect tensile strength and temperature distribution in 5052-H18 aluminum alloy friction stir welding. Boriwal et al. (2017) employed response surface design to predict shear and peel strength in dissimilar spot-welded joints based on welding parameters.

Due to the challenges in observing resistance spot welding (RSW) weld formation, inspections largely rely on destructive testing, which is inefficient and wasteful, with limited non-destructive alternatives (Zhang et al., 2019a; Gao et al., 2017, 2014). However, advancements in machine learning, particularly deep learning (DL) algorithms, show promise in addressing complex tasks like defect identification and diagnosis (Li et al., 2019; Gao et al., 2016). For example, Fu et al. utilized dynamic reactance signals and radar analysis charts in a CART model to predict weld strength (Fu et al., 2024). Despite these advancements, applying DL in this field remains challenging due to the large datasets typically required, while real-world scenarios often feature limited defect samples (Fan et al., 2022). Guo et al. improved RSW quality prediction using an LSTM network with infrared thermal videos, outperforming CNNs in both accuracy and computation time (Guo et al., 2022). Similarly, Quoc-Trinh Vo's team employed LSTM models based on RSW process parameters, achieving impressive results (MSE of 0.5, MAE of 0.25, and R^2 of 0.78) in weld quality prediction (Vo et al., 2023).

Various researchers have addressed the challenge of small sample sizes in fault diagnosis. Zhang et al. (2019b) proposed a semi-supervised multilayer network to manage limited labeled data. Wang (2023) utilized Improved Generative Adversarial Networks (IGAN) and Auto-Encoder models for assessing the quality of stainless steel spot welding, enhancing predictions even with small datasets. Geng et al. (2024) tackled the small-sample issue in automotive spot welding defect diagnosis using an improved DCGAN-VAE model, leveraging dynamic resistance curves to generate high-quality defect samples.

In addition to data-driven approaches, physically-based models that utilize finite element analysis (FEA) and thermoelectric coupling have been extensively applied to simulate heat generation, weld nugget growth, and defect formation during resistance spot welding (RSW) (Xia et al., 2023). While these models offer valuable mechanistic insights into the welding process, they often require extensive parameter calibration and significant computational resources, making them unsuitable for real-time defect detection. With the rapid advancement of artificial intelligence, deep learning and machine learning techniques have emerged as powerful tools for welding quality classification based on sensor data (Cheng et al., 2021; Zhang et al., 2023). For instance, Hu et al. (2024) investigated the application of Generative Adversarial Networks (GANs) to enhance and classify chip-cutting defect images, aiming to augment training data diversity and balance. They explored three GAN variants, DCGAN, CycleGAN, and StyleGAN3, for high-resolution image synthesis in visual inspection systems. Hsu and Liu (2021) proposed a multi-time series convolutional neural network (MTS-CNN) model for fault detection and diagnosis in semiconductor manufacturing, demonstrating effectiveness in identifying wafer defect patterns and detecting out-of-distribution wafer maps. Similarly, Kim et al. (2021) employed five deep learning models, VGGNet, ResNet18, ResNet34, MobileNetV2, and ShuffleNet, alongside multi-source domain adversarial training and cross-domain anomaly-aware contrastive learning to enhance the generalization capabilities of their models across domains.

While these methods effectively address challenges in defect recognition and critical sample size acquisition, they fall short in diagnosing defects in automotive body spot welding. Furthermore, these approaches are not linked to the underlying mechanisms of defect formation, limiting the depth of neural network applications in such discontinuous processes. To overcome issues such as high defect labeling costs, lengthy sampling periods, and difficulties in obtaining sufficient defect samples, particularly concerning the shunt effect—a novel approach is necessary. The shunt effect, which is more prevalent in three-layer welded plates than in burn-through or false welds, is often overlooked due to inadequate process control during production. This phenomenon significantly impacts weld quality, leading to weld strength degradation and, in some cases, complete weld failure.

In this paper, we propose a Generative Adversarial Network (GAN)-based method for detecting and identifying shunt defects in three-layer plate resistance spot welding. To determine the optimal welding parameters, we will conduct one-factor experiments utilizing Analysis of Variance (ANOVA) and Response Surface Methodology (RSM). These optimized parameters will then be applied in inter-plate shunt experiments, focusing on variables such as inter-plate gaps, oil contamination, and poor electrode surfaces. Additionally, we will collect dynamic resistance (DR) curves, which are closely linked to molten nugget formation. The Deep Convolutional Generative Adversarial Network-Conditional Variational Autoencoder (DCGAN-CVAE) model and Bidirectional Long Short-Term Memory network-One Dimensional Convolutional Neural Network (BiLSTM-1DCNN) algorithms will be employed for defect diagnosis in automotive body resistance spot welding.

2. Optimized parameter settings and defect samples for spot welding of three-layer plates

2.1. Experimental setup

The experimental system, as shown in Fig. 1, consists of a medium-frequency DC spot welding gun, a welding robot, and a cooling water tank. The RSW process requires real-time acquisition of welding current and electrode voltage signals. Key components include a three-phase AC power supply, an input rectifier, a bridge inverter, a welding transformer, and related equipment. Test electrodes are made from CuCrZr alloy with an end diameter of 6 mm. Current sensors, mounted on the electrostatic polearm, measure welding current, while shielded RF cables on the upper and lower electrodes measure electrode voltage. Fig. 1 (A) presents the metallographic diagram used to measure the molten core diameter, prepared with an EDM wire-cutting machine. This method involved cutting perpendicular to the welded joints' center and grinding and polishing after inlaying. The samples were then corroded using a four percent nitric acid alcoholic solution, allowing for observation of the welded joints' microstructure with a metallographic microscope. This analysis enabled the identification of different welding zones, including the fusion zone (FZ), heat-affected zone (HAZ), and base material (BM), with the diameter of the fusion core measured within the fusion core region.

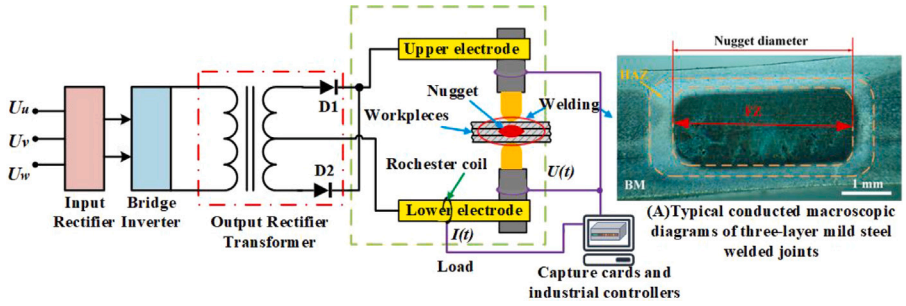

Fig. 1. Resistance spot welding equipment platform and schematic diagram.

2.2. Selection of optimal process parameters

This study investigates the influence of process parameters on the welding quality of three-layer resistance spot welded plates. A single-factor experimental method was employed to assess the individual effects of each parameter, providing foundational data for subsequent multi-factor optimization. DC01 mild steel, with a thickness of 1 mm per plate, was used for the experiments, focusing on welding current, welding time, and electrode pressure's effects on the diameter of the molten nucleus and the pulling shear strength. The pulling shear strength was measured using a universal pulling shear machine (Li et al., 2016), as shown in Fig. 2(A).

Experimental results in Fig. 2(B) indicate that welding current significantly affects both the molten core diameter and the tensile shear strength. As the welding current increases, the molten core diameter also increases due to enhanced Joule heating. However, excessively high currents (e.g., 12000 A) may lead to expulsion or burn-through, ultimately degrading the weld integrity and reducing tensile strength. Welding time similarly plays a critical role: longer durations allow more heat accumulation and growth of the fusion zone, thereby increasing the nugget diameter. Nevertheless, once the time exceeds 240 ms, thermal overload may occur, leading to microstructural degradation and a subsequent drop in tensile strength. In contrast, electrode pressure exhibits a relatively minor effect on nugget diameter, but significantly influences the mechanical strength by modulating the contact resistance and material flow. Higher electrode forces can stabilize the welding process, yet excessive pressure may suppress molten metal expansion and reduce the bonding area. In addition to weld quality, these parameter settings also affect the dynamic resistance (DR) signal characteristics, which are crucial for the performance of the data generation module. Specifically, higher currents and longer welding times tend to produce DR signals with stronger amplitude and clearer phase transitions, which enrich the training data for the generative model. Conversely, too low or extreme values may lead to insufficient signal diversity or poor feature quality, making it harder for the generation process to converge. Therefore, selecting representative parameter combinations ensures both the physical validity of the welds and the diversity of input signals used during data synthesis.

To quantitatively assess the impact of each process parameter on weld quality and explore interactions between parameters, a regression linear model was designed using Response Surface Methodology (RSM) in Design Expert software. This analysis utilized results from the one-factor experiments, employing a Central Composite Design (CCD) (Djoudi et al., 2007), as represented in Eq. (1).

$$\tilde{y} = \alpha_0 + \sum_{j=1}^{2n} a_j x_j^2 + \sum_{i=1}^{n-1} \sum_{j=i+1}^{n} a_{ij} x_i x_j \tag{1}$$

Where n is the number of independent variables, α_0 is the constant term, and α_j is the primary coefficient. The three process parameters of welding current (A), welding time (B) and electrode pressure (C) are used as input indicators to design three levels of three parameters based on the full response central composite design (CCD). The parameters and levels are designed as shown in Table 1.

Table 1
Process parameters and levels.

Process parameters	Level		
	-1	0	1
Welding current (kA)	8.5	9.5	10.5
Welding time (ms)	100	200	300
Electrode pressure (kN)	3	4	5

The software generated various parameter combinations for experimental data collection, which were analyzed using Analysis of Variance (ANOVA) to assess the significant effects of welding current, welding time, and electrode pressure on both the diameter of the molten nucleus and the pulling shear strength. The ANOVA results are summarized in Table 2.

Welding current and welding time significantly affected both the fusion core diameter and pulling shear strength ($p < 0.05$), while electrode pressure did not significantly influence the fusion core diameter but had a measurable impact on pulling shear strength. The welding current showed the largest F value, indicating it is the primary factor affecting welding quality. Therefore, welding current is identified as the most critical parameter for optimization, followed by welding time, with electrode pressure having the least impact.

Finally, response surface plots illustrating the relationships between different process parameters and weld quality are presented in Fig. 2(C). A quadratic polynomial model was constructed to represent the relationship between weld quality (both molten core diameter and tensile shear strength) and the process parameters of welding current, welding time, and electrode pressure as shown in Eq. (2). Based on the equipment conditions and experimental validation, optimal welding parameters of 9000 A, 250 ms, and 4 kN were selected for the next phase of defect fabrication.

$$\begin{aligned} D &= 5.60 + 0.1158I + 0.0521t - 0.0523F + 0.0113It \\ &\quad - 0.0338IF - 0.0100tF - 0.3022I^2 - 0.0173t^2 + 0.0559F^2 \\ F_s &= 7.55 + 0.1595I + 0.0718t - 0.0721F + 0.0155It \\ &\quad - 0.0465IF - 0.0138tF - 0.4163I^2 - 0.0239t^2 + 0.0770F^2 \end{aligned} \tag{2}$$

2.3. Defective sample production

The dynamic resistance signal reflects the evolution of both contact resistance and bulk resistance during the welding process. In RSW, the dynamic resistance curve is closely related to welding quality and defect evolution, and provides valuable diagnostic information on process stability. The dynamic resistance signal has been shown by most scholars to be closely related to weld quality (Zhou et al., 2020; Kang et al., 2025), as shown in Eq. (3).

$$R = (U - L * dI/dt)/I \tag{3}$$

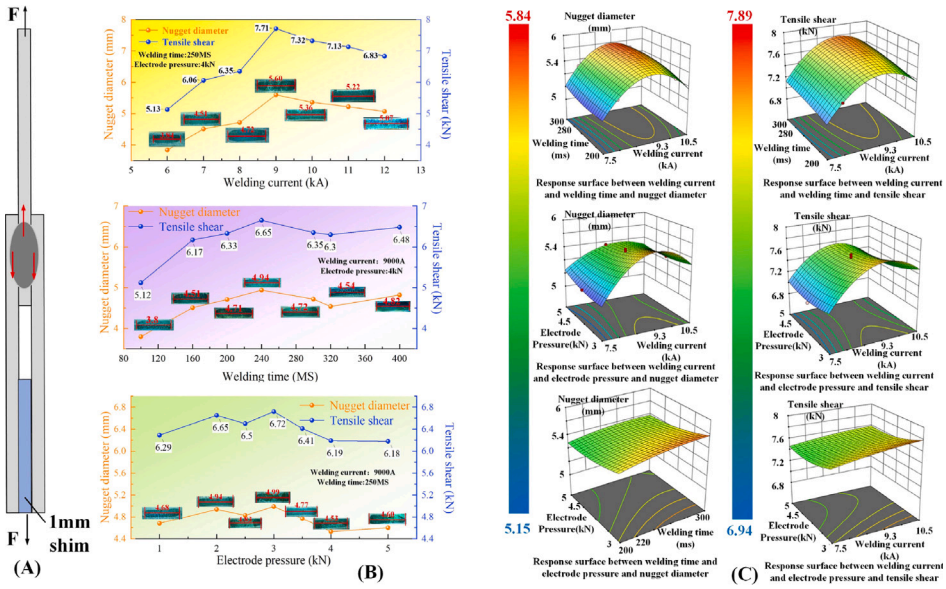

Fig. 2. Graphs of single-factor experimental results and multi-factor response surface analysis for resistance spot welding of three-layer boards.

Table 2
Second-order polynomial ANOVA table for the response as melt nugget diameter as well as tensile shear force (Nugget diameter/Tensile shear)

Source	Sum of Squares	df	Mean Square	F-value	p-value
Model (Quadratic model)	0.364/0.691	9	0.041/0.077	27.97	<0.0001 (significant)
A-Welding current	0.075/0.141	1	0.075/0.141	51.49	<0.0001 (significant)
B-Welding time	0.037/0.070	1	0.037/0.070	25.59	0.0005 (significant)
C-Electrode pressure	0.029/0.055	1	0.029/0.055	20.12	0.0012 (significant)
AB	0.001/0.001	1	0.001/0.001	0.311	0.5893 (not significant)
AC	0.004/0.008	1	0.004/0.008	2.80	0.1252 (not significant)
BC	0.001/0.002	1	0.001/0.002	0.553	0.4742 (not significant)
A^2	0.183/0.347	1	0.183/0.347	126.33	<0.0001 (significant)
B^2	0.005/0.009	1	0.005/0.009	3.18	0.1051 (not significant)
C^2	0.023/0.043	1	0.023/0.043	15.63	0.0027 (significant)
Residual	0.015/0.028	10	0.001/0.003		
Lack of Fit	0.010/0.019	5	0.002/0.004	2.23	0.2001 (not significant)
Pure Error	0.005/0.009	5	0.001/0.002		
Cor Total	0.379/0.719	19			

Where U is the electrode voltage, I is the welding current, L is the total inductance and R is the load resistance. $L * dI/dt$ is the induced voltage. Since the acquired raw signals have various noises, in this study, a second-order Chebyshev filter (Calvano et al., 2000) is used for noise reduction and enhancement, which has the advantages of steeper transition slopes in the pass-band and stop-band, higher selectivity and lower computational complexity.

The welding signals were acquired using a sensor-integrated welding platform that records dynamic resistance in real time throughout the welding process. To train and evaluate the defect classification system, we designed a set of controlled welding experiments to simulate common defect signals encountered in three-layer resistance spot welding. As shown in Fig. 3, nine types of weld results (both normal and defective) are defined, which form the basis of our dataset.

The nine welding outcome classes are as follows:

(1) Single Electrode Surface Defect. Covering single-side surfaces of steel plates with plastic film.

(2) Surface Defects on both Electrodes. Covering double-side surfaces of steel plates with plastic film.

(3) Upper-Middle Industrial-grade oil. Oil applied between the upper and middle steel plates.

(4) Middle-Lower Industrial-grade oil. Oil applied between the middle and lower steel plates.

(5) Industrial-grade oil present on All Layers. Oil all applied between the plates.

(6) Upper-Middle Gap. Glue foam adhesive between the upper and middle plates.

(7) Gaps in All Layers. Foam adhesive all applied between the plates.

(8) Middle-Lower Gap. Glue foam adhesive between the middle and lower plates.

(9) Normal welding. Welding without any defects with optimal parameters.

3. DCGAN-CVAE based identification model for resistance spot welding defect sample generation

While process optimization ensures proper welding quality and reliable dynamic resistance signals, the scarcity of real defective samples remains a major bottleneck for training robust classification models. To address this issue, we incorporate a generative model, DCGAN-CVAE, to synthesize high-fidelity dynamic resistance signals corresponding to various types of welding defects. This augmentation strategy not only balances the dataset, but also enhances the model's generalization capability for anomaly detection.

3.1. Overall structure of the model

The core idea of system is to use real dynamic resistance signals collected from controlled welding experiments covering both normal welds and several types of defects as the base dataset. However, since

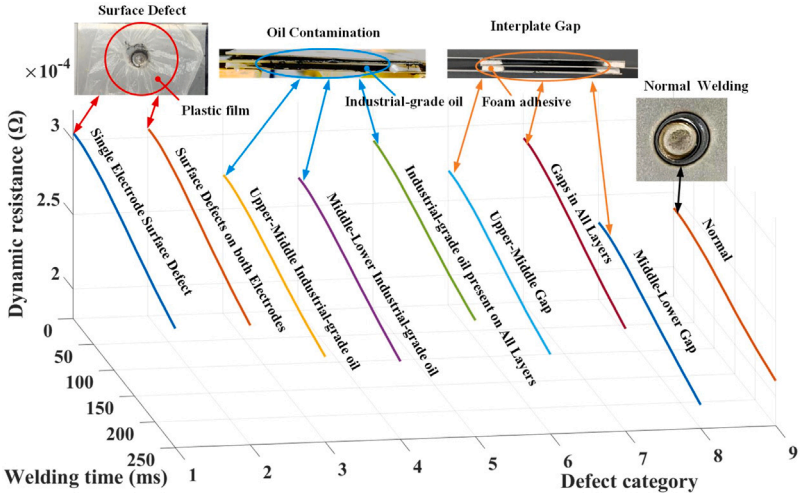

Fig. 3. Schematic diagram of dynamic resistance of different inter-board shunt effects for three-layer board resistance spot welding.

some defect types (e.g., oil contamination, electrode oxidation) are underrepresented, we apply a generative model (DCGAN-CVAE) to produce additional synthetic time-series samples for these classes. These generated samples are then combined with real data to train a robust classifier (BiLSTM-1DCNN), which improves generalization and handles class imbalance.

The model proposed in this study is illustrated in Fig. 4 and consists of three main modules: the data input processing module, the GAN-based defect sample generation model, and the BiLSTM-1DCNN classifier.

The data input processing module utilizes dynamic resistance signals collected during the welding process, formatted as time series data. Each defect sample corresponds to one row of data, with each column representing the dynamic resistance value recorded at 0.1 ms intervals. As such, the length of each resistance signal corresponds to the total number of time steps. The dimensions of the input data are $N \times T$, where N denotes the number of samples and T represents the number of time steps, i.e., the length of the resistance signal. To enrich the representation and enforce feature constraints, additional features, such as maximum value, mean, stable value, slope, and integral, are attached to each sample, as detailed in Table 3. The final column of each sample is labeled with the corresponding defect category.

The GAN-based defect sample generation model receives the processed data and trains the DCGAN-CVAE network to learn specific defect patterns and generate realistic defect-like signals. These generated samples are then integrated with real defect signals, along with the dynamic resistance signals of normal welds, and fed into the BiLSTM-1DCNN classifier. This hybrid classifier combines temporal feature extraction (via BiLSTM) with local pattern learning (via 1DCNN) to accurately identify both normal welds and a variety of defect types.

The other input consists of two elements: random noise and defect labels. The random noise, sampled from a standard normal distribution (mean 0, variance 1), introduces variability into the generation process. Defect labels provide the generator with information about the sample categories. These inputs are concatenated into a single vector, allowing the generated samples to be diverse while also producing specific defective types based on the given labels.

The classifier integrates a Bidirectional Long Short-Term Memory (BiLSTM) network (Graves et al., 2005) and a one-dimensional convolutional neural network (1DCNN) (Yang et al., 2022), with specific parameters listed in Table 5. Compared with traditional LSTM, BiLSTM has shown improved performance in capturing contextual dependencies in sequential data, which makes it well-suited for modeling time-dependent resistance signals. The BiLSTM outputs include both forward and backward hidden states, enabling the model to better understand temporal patterns. Detailed information about the network mechanism can be found in the literature (Kang et al., 2025).

The selected BiLSTM as the core sequence modeling component in the classification module, instead of a standard LSTM or GRU, based on its ability to capture both forward and backward temporal dependencies in time-series signals. To verify its effectiveness, we conducted a comparison experiment using the same training dataset with three variants. As shown in Table 4, BiLSTM outperformed both LSTM and GRU, leading to its final selection in our framework.

The one-dimensional convolutional neural network (1DCNN) is employed to extract local spatial features from dynamic resistance signals. Due to its sparse connections and shared weights, 1DCNN has been widely used in time series-based fault diagnosis tasks. To enhance feature extraction, we incorporate a residual module inspired by ResNet (He et al., 2016), forming a one-dimensional residual convolutional neural network architecture. This structure includes two branches: one with two consecutive one-dimensional convolutional layers and another with a shortcut connection that enables identity mapping. The output is obtained by summing the convolutional branch output with the residual path, followed by a ReLU activation. See the literature (Deng et al., 2024) for detailed mathematical calculations.

3.2. DCGAN-CVAE based defective sample generation model

GAN are known for their powerful data generation capabilities by learning data distributions through adversarial training (Gao et al., 2020). DCGAN (Dewi et al., 2022) extends the original GAN by incorporating convolutional structures, significantly enhancing generation quality. It comprises two competing networks: a generator that produces synthetic samples and a discriminator that distinguishes real from fake samples. The training process follows the standard min–max game framework introduced in the literature (Dewi et al., 2022).

The structure of the DCGAN-CVAE model used in this study is shown in Fig. 5. The activation function of the unlabeled convolutional layer defaults to $ReLU()$, while the activation function of the fully connected layer defaults to $sigmoid()$. Specific structural parameters are detailed in Table 6. The Conditional Variational Autoencoder (CVAE) (Liu et al., 2022) serves as the core architecture of the generator. It consists of an encoder that transforms input data into a latent representation and a decoder that reconstructs the input conditioned on both the latent vector and class label. This enables the model to generate defect-specific resistance signals based on category information. The training follows the standard variational inference framework. For a detailed probabilistic formulation, see the literature (Liu et al., 2022).

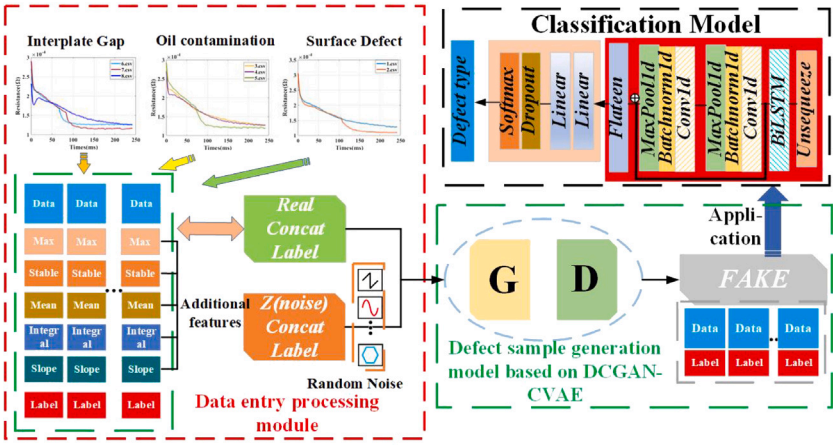

Fig. 4. Structural flowchart of DCGAN-CVAE based resistance spot welding defect sample generation recognition model.

Table 3
Description of additional features for model inputs.

Additional features	Explanation
Max Value	The maximum resistance value in the resistance curve, which indicates the peak value of resistance during the welding process, is usually associated with the heating phase of the welding process.
Stable Value	The average value of the stabilization phase at the end of the resistance curve is taken as the mean value of the 10 points at the end of the curve, reflecting the stabilized state of the resistance at the end of the weld.
Mean Value	The average of the entire resistance curve, indicating the overall level of resistance during the welding process.
Integral Value	The integral of the resistance curve, which represents the cumulative effect of resistance during the welding process, is commonly used as a measure of welding power consumption.
Slope	The slope of the entire resistance curve is calculated by linear regression, reflecting the overall trend of resistance during the welding process.

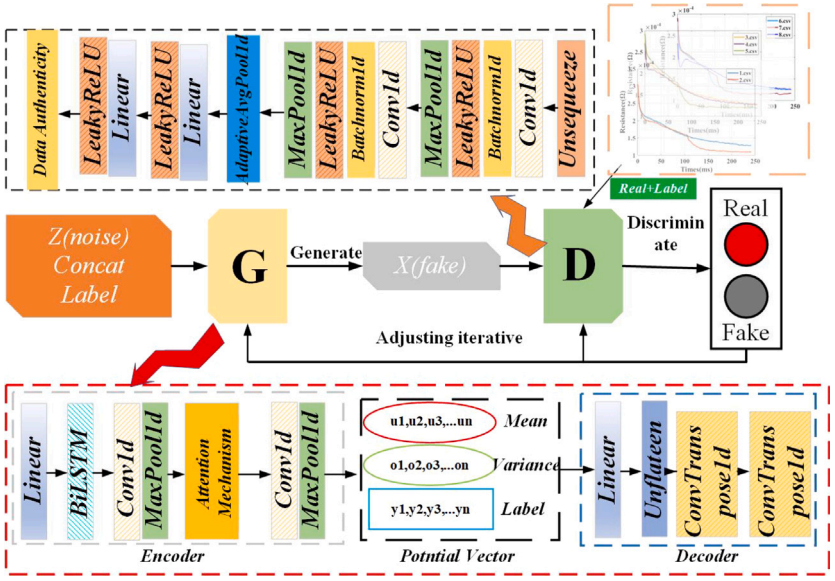

Fig. 5. Schematic structure of the dynamic resistive characterization of interplate shunt defects based on DCGAN-CVAE data enhancement.

The objective function of the CVAE model mainly consists of a reconstruction error term and a regularization term as shown in Eq. (4).

$$\min L_{CVAE} = \frac{1}{N_h}\sum \left(\boldsymbol{X} - D_c\left(\boldsymbol{y}, E_c(\boldsymbol{y}, \boldsymbol{X})\right)\right)^2 + \beta D_{\mathrm{KL}}(q(z \mid \boldsymbol{y}, \boldsymbol{X}) \| p(z \mid \boldsymbol{y})) \tag{4}$$

Where N_b is the number of single training samples, the function D_{KL} is the relative entropy, also known as KL divergence, which is used to measure the degree of difference between two probability distributions, and β is the weight parameter of the K–L divergence term.

To improve the quality and diversity of generated dynamic resistance signals, we propose a hybrid generation model that combines

Table 4
Model accuracy comparison.

Model	Accuracy (%)
LSTM	90.86
GRU	91.51
BiLSTM	94.44

Table 5
Description of additional features for model inputs.

Layers	Input	Output	Other parameters
BiLSTM	1 × 256	256 × 256	hidden_dim = 128
Conv1d_1	256 × 256	64 × 256	kernel_size = 3, padding = 1
MaxPool1d_1	64 × 256	64 × 64	kernel_size = 4
Conv1d_2	64 × 64	64 × 64	kernel_size = 3, padding = 1
MaxPool1d_2	64 × 64	64 × 16	kernel_size = 4
Flatten	66560 × 1	66 560	
fc_1	66 560	128	
fc_2	128	9	Classification as 9
Softmax	9	9	Output

Table 6
Network architecture parameters for DCGAN-CVAE data enhancement modeling.

Module	Layers	Input	Output	Other parameters
G	BiLSTM	256 × 1	256 × 256	hidden_dim = 128
	Conv1d_1	256 × 256	64 × 256	kernel_size = 3, padding = 1
	MaxPool1d_1	64 × 256	64 × 64	kernel_size = 4
	Self_Attention	64 × 64	64 × 64	h = 4
	Conv1d_2	64 × 64	64 × 64	kernel_size = 3, padding = 1
	MaxPool1d_2	64 × 64	64 × 16	kernel_size = 4
	ConvTranspose1d_1	64 × 16	64 × 16	kernel_size = 3, padding = 1
	ConvTranspose1d_2	64 × 16	256 × 16	kernel_size = 3, padding = 1
D	Conv1d_1	1 × 256	64 × 256	kernel_size = 3, padding = 1
	MaxPool1d_1	64 × 256	64 × 64	kernel_size = 4
	Conv1d_2	64 × 64	64 × 64	kernel_size = 3, padding = 1
	MaxPool1d_2	64 × 64	64 × 16	kernel_size = 3, padding = 1
	AdaptiveAvgPool1d	64 × 16	64 × 1	
	fc_1	64	128	
	fc_2	128	1	

the strengths of Conditional Variational Autoencoder (CVAE) and Deep Convolutional GAN (DCGAN). This synergy leverages the structured latent sampling and controllability of CVAE and the realism and sharpness of GAN-generated outputs. While CVAE ensures that the generation is conditioned and consistent with physical features, GAN promotes realistic waveform morphology through adversarial learning. Together, the DCGAN-CVAE architecture enables both accurate and high-fidelity defect signal generation for data augmentation.

In this study, the proposed DCGAN-CVAE model is applied not to image data, but rather to dynamic resistance time-series signals collected during the resistance spot welding (RSW) process. The primary objective of this module is to generate synthetic defective samples, which are typically difficult to acquire in real-world production settings due to safety concerns, high costs, and significant data imbalance across defect categories. Specifically, the generator learns to produce time-series resistance patterns that resemble known defective types, while the discriminator is trained to distinguish between real and synthetic samples. These generated defective samples are then utilized to augment the training dataset of a downstream BiLSTM-1DCNN classifier, enhancing its training diversity and generalization capability.

This data augmentation strategy effectively mitigates the class imbalance problem, particularly for rare defect types, and improves the robustness of the defect detection model. Furthermore, the integration of a CVAE with DCGAN enables the generation of resistance signals with greater feature continuity and diversity, ensuring the synthetic samples better reflect the complex dynamics of real welding defects.

3.3. Algorithm implementation process

To address the challenges of small-sample learning and data imbalance in RSW defect detection, we propose a hybrid generation-and-classification framework. The system consists of two key components: (1) a generative model based on DCGAN-CVAE, and (2) a BiLSTM-1DCNN classifier for identifying welding defects. The input to the framework is a time-series signal of dynamic resistance, which captures the evolution of electrical and thermal characteristics throughout the welding process. In the first stage, the DCGAN-CVAE module learns the underlying distribution of real resistance curves and generates high-fidelity synthetic samples that represent various defect types. These generated samples supplement the limited real-world data and help mitigate the class imbalance problem, especially for rare defect categories. In the second stage, both real and synthetic signals are input to a classification network that integrates BiLSTM units with one-dimensional convolutional layers. This architecture effectively captures long-range temporal dependencies and local structural features from the resistance signals, resulting in enhanced defect detection accuracy. The model described is represented in Eq. (5). The algorithm workflow process is illustrated in Fig. 6.

$$\begin{aligned} R(\text{real}) &= \left[r^1\left(t_s\right)^{SG}, \ldots, r^{\text{index}}\left(t_s\right)^{SG}\right], \\ R(\text{fake}) &= \left[r^1_{\text{fake}}, r^2_{\text{fake}}, \ldots, r^n_{\text{fake}}\right], \\ R(\text{All}) &= R(\text{real}) + R(\text{fake}), \\ D_{\text{type}} &= f(R(\text{All})) \end{aligned} \tag{5}$$

Where $\left[r^1\left(t_s\right)^{\text{SG}}, \ldots, r^{\text{index}}\left(t_s\right)^{\text{SG}}\right]$ represents the real dataset, $\left[r^1_{\text{fake}}, r^2_{\text{fake}}, \ldots, r^n_{\text{fake}}\right]$ represents the GAN training output with R (real) size consistent with the augmented dataset, R (All) represents the entire dataset trained by the model in this paper, and D_{type} represents the predicted output of the welding nugget anomaly type of the model.

4. Implementation and effectiveness of resistance spot welding detection method based on DCGAN-CVAE

4.1. Comparative test of data generation

The dataset consists of 740 real samples, including 500 samples of normal parameter welds (classification number 9) and 240 samples of defective welds. The defective samples were further divided into 30 samples for each of the two surface oxidation conditions and 30 samples for each of the three interplate gap and oil contamination conditions. These samples were tested under controlled experimental conditions using a multi-layer DC01 steel configuration. Defects were intentionally introduced by:

Surface defect: Covering the surface of the steel plate with plastic film, divided into single-side and double-side coverings, with classification numbers corresponding to 1 (single side), 2 (double-side).

Oil contamination: A thin layer of industrial-grade oil is applied between the plates before welding, divided into the upper and middle layers applied, the middle and lower layers applied and all applied between the plates, corresponding to the classifications numbered 3,4,5.

Interplate gap: Insertion of foam adhesive (2 mm) to simulate improper contact, classified as upper-middle insertion, lower-middle insertion and full insertion between panels, corresponding to classification numbers 6,7,8.

Additionally, Fig. 3 illustrates a representative visual example of each defect.

The dynamic resistance curves obtained from the experimental samples above were used to remove outliers and sensor drift using a second-order Chebyshev filter (Calvano et al., 2000) and normalize all signals to zero mean and unit variance, which were then fed into the generation and classification models. 240 defect datasets were fed into the DCGAN-CVAE model for generating the trainer, generating 500

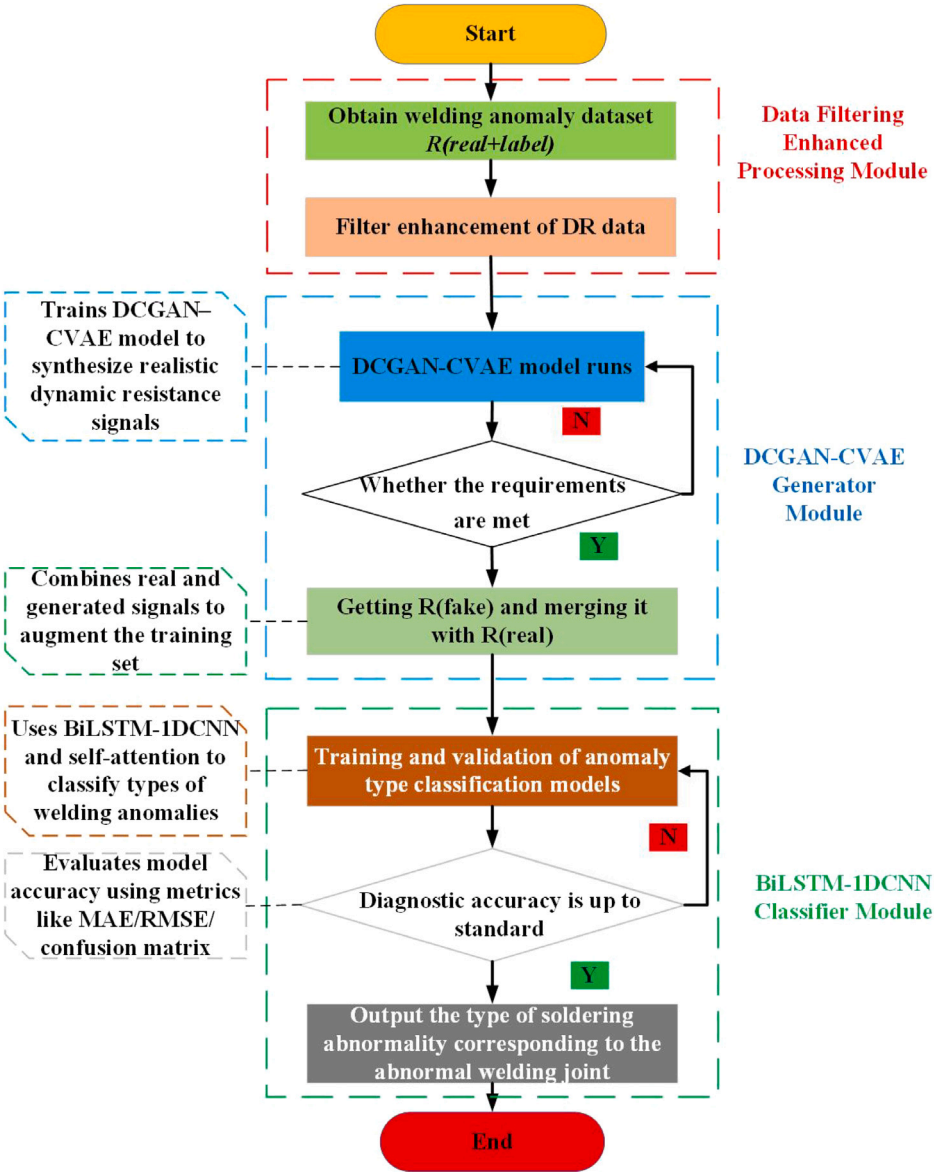

Fig. 6. Algorithm schematic of DCGAN-CVAE based algorithm for enhanced generation and recognition of resistance spot welding data.

defect samples by their respective categories for a total of 4500 data. Combined with 500 normal welding data, a total of 5000 data were input into the classifier for recognition, whose specific deep learning, neural network structure, and hyperparameters are shown in Table 7.

The model's performance was evaluated using three similarity-based statistical metrics : Kullback–Leibler Scatter (K–L), Pearson's Correlation Coefficient (PCC), and Euclidean Distance (ED) to assess the quality of the generated samples (Gutiérrez et al., 2023). In our experiments: K–L divergence values below 0.15 typically indicate close alignment in probability distribution between real and generated signals. PCC values above 0.80 correspond to strong similarity in waveform trends, suitable for training reliable classifiers. ED values below 0.1 reflect low average point-wise error in amplitude, signifying high-fidelity signal reconstruction. These thresholds were empirically derived from multiple trials and reflect a balance between signal realism and classification utility.

The Kullback–Leibler (K–L) divergence (Erven and Harremos, 2014) is a statistical measure of the difference between two probability distributions. In this context, it quantifies how much the distribution of generated signals deviates from that of real signals. A smaller KL value indicates higher similarity, as shown in Eq. (6).

$$KL(\text{Generated}\|\text{Real}) = \sum_{x\in X} \text{Generated}(x) \log \frac{\text{Generated}(x)}{\text{Real}(x)} \tag{6}$$

Where Real is the distribution of real samples of spot welding defects, and Generated is the distribution of samples generated by the model.

The Pearson correlation coefficient (PCC) (Cohen et al., 2009) measures the linear correlation between two time series. Values close to 1 indicate that the generated and real signals follow very similar trends. PCC can be used to reflect the correlation between two variables x and y. The more correlated the absolute values are, the stronger the similarity is when the PCC value is greater than 0.8, as shown in Eq. (7).

$$r = \frac{\sum_{i=1}^{n}(x_i-\bar{x})(y_i-\bar{y})}{\sqrt{\sum_{i=1}^{n}(x_i-\bar{x})^2}\sqrt{\sum_{i=1}^{n}(y_i-\bar{y})^2}} = \frac{\sum x_i y_i - n\bar{x}\bar{y}}{\sqrt{(\sum x_i^2 - n\bar{x}^2)}\sqrt{(\sum y_i^2 - n\bar{y}^2)}} \tag{7}$$

The Euclidean Distance (ED) (Dokmanic et al., 2015) is a measure of the absolute distance between two points in a multidimensional space,

Table 7
Architectural and training hyperparameters of the DCGAN-CVAE framework.

Module	Layer	Type	Output Size	Activation
CVAE Encoder	Input	–	1 × 1000	–
	Conv1D	Convolution	64 channels	ReLU
	MaxPool1D	Pooling	64 channels	–
	FC	Dense Layer	128	ReLU
	Latent Vector	Dense Layer	32	Linear
CVAE Decoder	FC	Dense Layer	128	ReLU
	Upsample + Conv1D	Deconv Layer	64 channels	ReLU
	Output	Conv1D	1 × 1000	Tanh
DCGAN Generator	Input Noise z	–	100-dim vector	–
	FC	Dense Layer	256	LeakyReLU
	ConvTranspose1D	Deconv Layer	64 channels	LeakyReLU
	Output	Conv1D	1 × 1000	Tanh
DCGAN Discriminator	Conv1D	Convolution	64 channels	LeakyReLU
	FC	Dense Layer	1 (binary output)	Sigmoid
Classifier	BiLSTM	2-layer LSTM	Hidden size = 64	–
	1D-CNN	Convolution	128 channels	ReLU
	FC	Dense Layer	9 classes	Softmax
Deep Learning Settings				
GAN & CVAE: Adam optimizer, learning rate = 0.0002, batch size = 32, epochs = 1000				
Classifier: SGD optimizer, learning rate = 0.001, batch size = 32, epochs = 500				

Table 8
Evaluation results of similarity between real and generated samples across eight defect types.

Defect type	KL divergence	PCC	Euclidean distance
Single Electrode Surface Defect	0.0398	0.9632	0.0654
Surface Defects on both Electrodes	0.0431	0.9608	0.0667
Upper-Middle Industrial-grade oil	0.0475	0.9589	0.0681
Middle-Lower Industrial-grade oil	0.0407	0.9602	0.0632
Industrial-grade oil present on All Layers	0.0354	0.9648	0.0615
Upper-Middle Gap	0.0420	0.9610	0.0651
Gaps in All Layers	0.0417	0.9597	0.0643
Middle-Lower Gap	0.0389	0.9637	0.0639

and for a dynamic resistance curve, as shown in Eq. (8), the smaller the value, the stronger the correlation.

$$ED(x, y) = \sqrt{\sum_{i=1}^{2} (x_i - y_i)^2} \tag{8}$$

Eight defective samples were generated using the models to calculate their respective K–L divergence, PCC, and ED, presented in Table 8.

The results indicate that the improved DCGAN-CVAE algorithm proposed in this paper demonstrates a clear advantage over other generative models, particularly in the PCC and ED metrics, which are close to 1 and 0, respectively, when compared with other models. This finding confirms that the generated samples exhibit higher quality and greater similarity to the training samples, leading to superior metric scores and demonstrating the algorithm's enhanced sample reconstruction performance.

Additionally, to visually assess the fidelity of the generated samples, Fig. 7 illustrates several synthetic dynamic resistance curves generated by the DCGAN-CVAE model for three different weld defect types. Among them, the generated curves with subtle multi-peak oscillations are indicated in (a), which corresponds to the inconsistency of current conduction caused by oxidation or roughness of the electrode surface; the generated samples in (b) show a smooth low-amplitude resistance trend, which reflects the insulating effect of the oil film on the contact resistance; and the generated curves with subtle multi-peak oscillations are indicated in (c), which corresponds to the inconsistency of current conduction caused by oxidation or roughness of the electrode surface. The dynamic resistance curve of a normal solder joint is shown in (d).

It can be observed that the generated signals not only maintain the overall structural characteristics of real resistance signals – such as peak amplitude, slope variation, and final convergence – but also preserve defect-specific patterns. Notably, each defect category shows distinguishable waveform trends, demonstrating that the model successfully captures inter-class differences. This visual evidence complements the quantitative evaluation metrics (K–L divergence, PCC, ED) and reinforces the effectiveness of the proposed generative method.

Table 9
Comparison of parameter settings for different resistance spot welding modeling algorithms.

Method	Parameter	Value
CNN, LSTM, GRU, BiLSTM-1DCNN	Epochs	500
	Batch size	10
	Learning rate	0.001
	Optimizer	Adam
	Loss function	Binary cross entropy
SVM	C	1.0
	gamma	scale

4.2. Evaluation of classification results

To avoid data leakage, we ensured that the generated samples used for testing were produced from a disjoint set of original defect samples that were not used during training. Specifically, we divided the 30 original real samples for each defective category into two groups: 20 samples were used to generate 400 synthetic samples for training, and the remaining 10 real samples were used to generate 100 synthetic samples for testing. The 500 normal samples were then also similarly divided into two groups: 400 samples for training and the remaining 100 samples for testing. The specific parameters of the classifier are shown in Table 9. This ensures that no synthetic test sample is derived from the same source as those in training, maintaining independence between training and validation data.

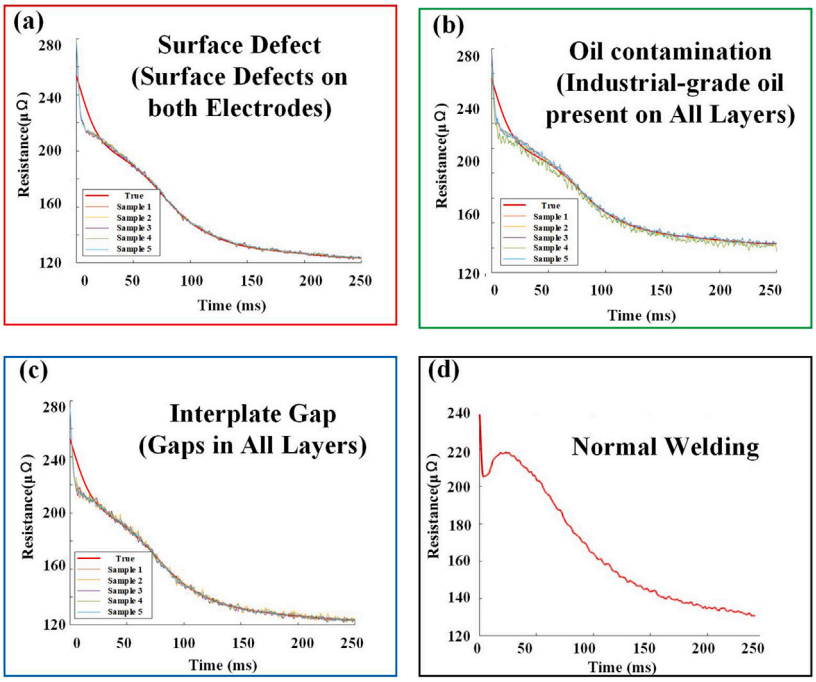

Fig. 7. Comparison of dynamic resistance data generation for different defects based on DCGAN-CVAE generative modeling. (Samples 1 to 5 are generated by the DCGAN-CVAE model).

The confusion matrix results, shown in Fig. 8, indicate that the BiLSTM-1DCNN model has very low recognition errors when identifying defects related to the interplate shunt. Misclassified samples primarily belong to the same class of inter-plate defects, including poor indication, inter-plate gaps, and inter-plate oil contamination. Notably, the defects related to interplate gaps and oil stains often overlap within the same class of interplate defects, demonstrating the model's ability to effectively recognize normal samples as well. In particular, the interplate gap and oil contamination defects are occasionally misclassified as one another. This is likely due to their similar effects on the mid-phase of the dynamic resistance (DR) signal, where both tend to produce delayed or flattened resistance peaks as a result of poor electrical contact. The surface defect class also shows partial confusion with the oil contamination class, likely because both introduce non-uniform current flow paths, causing irregularities in the early rising edge of the DR curve. Additionally, some mild shunt cases are misidentified as normal welds due to subtle signal distortions that remain within the statistical variance range of normal samples, especially when the shunt is weak or localized. This highlights the challenge of distinguishing physically subtle but mechanically significant defects, particularly when class boundaries are blurred in the feature space. These misclassifications suggest that further refinement, such as the use of domain-informed features, adaptive thresholds, or attention-based weighting, may improve classification robustness.

Compared with other algorithms, the accuracy of the proposed method's test set is shown in Fig. 9. The average accuracy achieved by this paper's algorithm is 98.7%, while the average accuracies of SVM, GRU, BiLSTM, and 1DCNN are 80.1%, 84.3%, 87.0%, and 91.7%, respectively. This represents a significant improvement over traditional deep learning algorithms and demonstrates superior classification performance.

From the overall average of all generated defect classes, a comparative study was conducted between the proposed DCGAN-CVAE model and three commonly used generative baselines: CVAE, DCGAN, and VAE-GAN. We evaluated each model using the three similarity metrics (K–L divergence, Pearson correlation coefficient, and Euclidean distance) and examined the effect of generated samples on classification performance. The results, shown in Table 10, demonstrate that DCGAN-CVAE achieves the best signal fidelity and downstream accuracy, highlighting the advantage of combining latent structure conditioning (CVAE) with adversarial learning (GAN) for time-series generation.

To evaluate the generalization capability of the proposed DCGAN-CVAE-based classification system in real-world applications, we designed a control experiment using real defect samples as the exclusive testing set. As shown in Table 11, the model trained only on real data achieved an accuracy of 88.54%. When trained with both real and synthetic data and tested on real data, accuracy increased to 96.27%, indicating that synthetic samples contributed positively to model generalization. Meanwhile, the model trained and tested solely on synthetic data achieved 98.73% accuracy. While this reflects internal consistency, real-only testing remains a better indicator of practical applicability. The results demonstrate that the proposed system not only performs well on generated data but also maintains high accuracy in real-world scenarios, validating its industrial potential.

To assess the scalability of the proposed approach for industrial application, we evaluated the training and inference efficiency of the DCGAN-CVAE and BiLSTM-1DCNN components. The full model requires approximately 5 h of training time for 1000 epochs on a standard GPU, which is feasible for offline retraining. Once trained, the model can generate over 1000 synthetic signals in less than 10 s, supporting real-time data augmentation. The classification model processes each test sample in under 20 ms, making it suitable for online inference during production. Memory usage remains within reasonable bounds (under 4 GB during generation and classification combined), and the framework can be further optimized for deployment on edge computing platforms through quantization or pruning techniques. These properties demonstrate that the proposed method is scalable, lightweight, and promising for practical industrial integration.

In many instances, the lack of augmented anomalous feature data and insufficient numbers and types of training datasets hinder the effectiveness of most deep learning methods in identifying and diagnosing welding core anomalies. The combination of the DCGAN-CVAE generative model with the BiLSTM-1DCNN algorithm shows that both the quantity and quality of key samples significantly influence predictive capability.

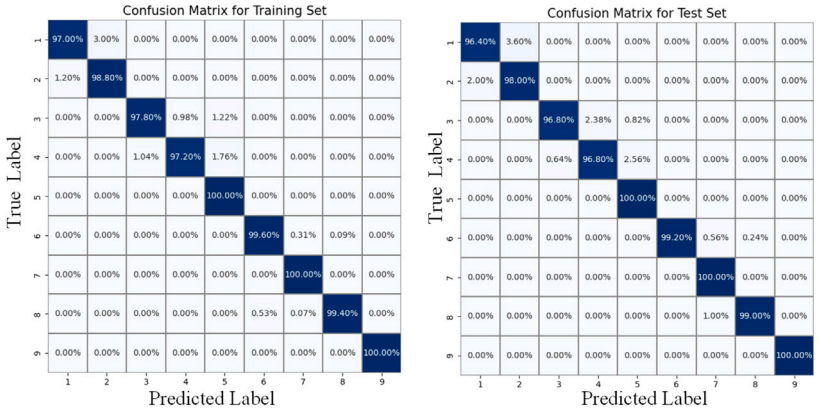

Fig. 8. Confusion matrix for model training set and test set recognition classification of BiLSTM-1DCNN.

Table 10
Performance comparison of generative models on signal similarity and classification accuracy.

Model	K–L divergence	PCC	ED	Classification accuracy (%)
CVAE (Liu et al., 2022)	0.0634	0.9212	0.0973	91.42
DCGAN (Dewi et al., 2022)	0.0597	0.9345	0.0821	92.85
VAE-GAN (Bao et al., 2017)	0.0551	0.9487	0.0776	94.76
DCGAN-CVAE (Ours)	**0.0413**	**0.9618**	**0.0645**	**98.73**

Table 11
Performance comparison of different training data configurations.

Training data	#Samples (Train)	Testing data	#Samples (Test)	Accuracy (%)
Real Only	400 normal + 160 defect	Real Only	100 normal + 80 defect	88.54
Real + Synthetic	400 normal + 3200 defect	Real + Synthetic	100 normal + 800 defect	98.73
Real + Synthetic	400 normal + 3200 defect	Real Only	100 normal + 80 defect	96.27

Note: Synthetic are generated using the DCGAN-CVAE model to balance the underrepresented defect classes. We divided the 30 original real samples for each defective category into two groups: 20 samples were used to generate 400 synthetic samples for training, and the remaining 10 real samples were used to generate 100 synthetic samples for testing. The real-only test set contains 10 samples per defect class.

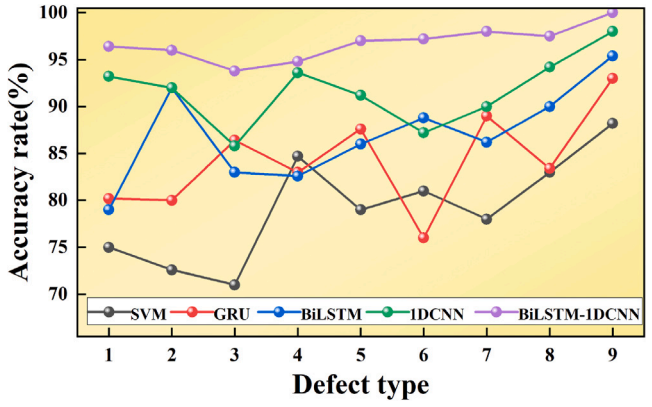

Fig. 9. Comparison plot of the accuracy of different resistance spot welding algorithms on the test set.

5. Conclusion

This paper presents a defect sample generation and classification method utilizing DCGAN-CVAE to address welding defects arising from the inter-plate shunt effect in resistance spot-welded three-layer plates. Optimized welding parameters were determined through one-factor experiments, supplemented by ANOVA and response surface analysis. Dynamic resistance signals were collected based on these parameters during inter-plate shunt experiments. The DCGAN-CVAE model successfully generated a multitude of simulated defect samples that closely resemble real defect samples in terms of feature dimensions. Classification tests on these generated samples demonstrated significant improvements in accuracy, validating the effectiveness and reliability of the generation model. This approach effectively increases the availability of defect samples and addresses the challenge of limited real defect samples, providing new data support and optimization pathways for welding quality control. Importantly, additional control experiments showed that the classifier trained with synthetic and real data maintained a 96.27% accuracy when tested exclusively on real defect signals, demonstrating the potential practical viability of our system in realistic manufacturing environments.

While the proposed approach demonstrates strong performance in detecting shunt defects in three-layer low-carbon steel resistance spot welding, there are several avenues worth exploring in future work. First, although the current framework achieves efficient inference, its applicability in real-time industrial scenarios could be further enhanced through lightweight model optimization or deployment on edge computing platforms. Second, this study focuses on a specific material configuration (DC01 steel). Extending the method to different materials, such as high-strength steels or aluminum alloys, would help assess its generalizability across various welding conditions. Future research will also explore integrating adaptive learning strategies and physics-informed models to further improve robustness, interpretability, and scalability in more complex manufacturing environments.

CRediT authorship contribution statement

Haofeng Deng: Writing – review & editing, Writing – original draft, Supervision, Methodology, Investigation, Formal analysis, Conceptualization. **Xiangdong Gao:** Writing – review & editing, Validation, Project administration, Funding acquisition, Data curation. **Dongfang Zhang:** Writing – original draft, Validation, Supervision, Software, Methodology, Investigation, Formal analysis. **Wuqi Lu:** Writing – original draft, Validation, Resources, Methodology, Investigation, Formal analysis. **Pengyu Gao:** Writing – review & editing, Supervision, Project administration, Funding acquisition, Data curation. **Yanxi Zhang:** Writing – review & editing, Validation, Project administration, Investigation, Funding acquisition, Data curation.

Funding

Funding was received from the Production and Research Project (No. 23HK0610), the Guangdong Provincial Natural Science Foundation of China under Grant 2023A1515012172, the Guangzhou Municipal Special Fund Project for Scientific and Technological Innovation and Development under Grant 2023B03J1326.

Declaration of competing interest

The authors declare that they have no known competing financial interests or personal relationships that could have appeared to influence the work reported in this paper.

Acknowledgments

This work was supported by the Production and Research Project (No. 23HK0610), the Guangdong Provincial Natural Science Foundation of China under Grant 2023A1515012172, and the Guangzhou Municipal Special Fund Project for Scientific and Technological Innovation and Development under Grant 2023B03J1326.

Data availability

The data are not publicly available due to privacy or ethical restrictions.

References

Bao, Jianmin, Chen, Dong, Wen, Fang, Li, Houqiang, Hua, Gang, 2017. CVAE-GAN: fine-grained image generation through asymmetric training. In: Proceedings of the IEEE International Conference on Computer Vision. pp. 2745–2754.

Boriwal, L., Sarviya, R.M., Mahapatra, M.M., 2017. Optimization of weld bonding process parameters of austenitic stainless steel 304L and low carbon steel sheet dissimilar joints. J. Adhes. Sci. Technol. 31 (14), 1591–1616.

Calvano, José Vicente, Alves, Vladimir Castro, Lubaszewski, Marcelo, 2000. Fault detection methodology and BIST method for 2nd order butterworth, Chebyshev and bessel filter approximations. In: Proceedings 18th IEEE VLSI Test Symposium. pp. 319–324.

Chen, Geng, Sheng, Buyun, Luo, Ruipin, Jia, Pengzhen, 2022a. A parallel strategy for predicting the quality of welded joints in automotive bodies based on machine learning. J. Manuf. Syst. 62, 636–649.

Chen, Wei-Hsin, Uribe, Manuel Carrera, Kwon, Eilhann E., Lin, Kun-Yi Andrew, Park, Young-Kwon, Ding, Lu, Saw, Lip Huat, 2022b. A comprehensive review of thermoelectric generation optimization by statistical approach: Taguchi method, analysis of variance (ANOVA), and response surface methodology (RSM). Renew. Sustain. Energy Rev. 169, 112917.

Cheng, Ken Chau-Cheung, Chen, Leon Li-Yang, Li, Ji-Wei, Li, Katherine Shu-Min, Tsai, Nova Cheng-Yen, Wang, Sying-Jyan, Huang, Andrew Yi-Ann, Chou, Leon, Lee, Chen-Shiun, Chen, Jwu E., et al., 2021. Machine learning-based detection method for wafer test induced defects. IEEE Trans. Semicond. Manuf. 34 (2), 161–167.

Cohen, Israel, Huang, Yiteng, Chen, Jingdong, Benesty, Jacob, Benesty, Jacob, 2009. Pearson correlation coefficient. In: Noise Reduction in Speech Processing. pp. 1–4.

Dai, Wei, Li, Dayong, Zheng, Yongjia, Wang, Dong, Tang, Ding, Wang, Huamiao, Peng, Yinghong, 2022. Online quality inspection of resistance spot welding for automotive production lines. J. Manuf. Syst. 63, 354–369.

Deng, Haofeng, Gao, Xiangdong, Lv, Zigui, Tan, Wenzheng, Gao, Pengyu, 2024. Study of spot distance on resistance spot welding quality: a 1DCNN-BiLSTM-Attention-based online inspection method. Meas. Sci. Technol. 36 (1), 015133.

Dewi, Christine, Chen, Rung-Ching, Liu, Yan-Ting, Tai, Shao-Kuo, 2022. Synthetic data generation using DCGAN for improved traffic sign recognition. Neural Comput. Appl. 34 (24), 21465–21480.

Djoudi, W., Aissani-Benissad, Farida, Bourouina-Bacha, Saliha, 2007. Optimization of copper cementation process by iron using central composite design experiments. Chem. Eng. J. 133 (1–3), 1–6.

Dokmanic, Ivan, Parhizkar, Reza, Ranieri, Juri, Vetterli, Martin, 2015. Euclidean distance matrices: essential theory, algorithms, and applications. IEEE Signal Process. Mag. 32 (6), 12–30.

Erven, Tim Van, Harremos, Peter, 2014. Rényi divergence and Kullback–Leibler divergence. IEEE Trans. Inform. Theory 60 (7), 3797–3820.

Fan, Xi'an, Gao, Xiangdong, Zhang, Nanfeng, Ye, Guangwen, Liu, Guiqian., Zhang, Yanxi, 2022. Monitoring of 304 austenitic stainless-steel laser-MIG hybrid welding process based on EMD-SVM. J. Manuf. Process. 73, 736–747.

Fu, Yan, Gao, Perry P., Gao, Xiangdong, Zhang, Yanxi, 2024. Quality evaluation of resistance spot welding based on dynamic reactance signal and rader diagram method. IEEE Sensors J. 24, 6666–6676.

Gao, Yiping, Gao, Liang, Li, Xinyu, 2020. A generative adversarial network based deep learning method for low-quality defect image reconstruction and recognition. IEEE Trans. Ind. Inform. 17 (5), 3231–3240.

Gao, Xiangdong, Liu, Yonghua, You, Deyong, 2014. Detection of micro-weld joint by magneto-optical imaging. Opt. Laser Technol. 62, 141–151.

Gao, Xiangdong, Mo, Ling, You, Deyong, Li, Zhuman, 2017. Tight butt joint weld detection based on optical flow and particle filtering of magneto-optical imaging. Mech. Syst. Signal Process. 96, 16–30.

Gao, Xiangdong, Sun, Yan, You, Deyong, Xiao, Zhenlin, Chen, Xiaohui, 2016. Multisensor information fusion for monitoring disk laser welding. Int. J. Adv. Manuf. Technol. 85, 1167–1175.

Geng, Chen, Buyun, Sheng, Gaocai, Fu, Xiangxiang, Chen, Guangde, Zhao, 2024. A GAN-based method for diagnosing bodywork spot welding defects in response to small sample condition. Appl. Soft Comput. 157, 111544.

Graves, Alex, Fernández, Santiago, Schmidhuber, Jürgen, 2005. Bidirectional LSTM networks for improved phoneme classification and recognition. In: International Conference on Artificial Neural Networks. pp. 799–804.

Guo, Shenghan, Wang, Dali, Chen, Jian, Feng, Zhili, Guo, Weihong Grace, 2022. Learning the temporal effect in infrared thermal videos with long short-Term memory for quality prediction in resistance spot welding. In: International Manufacturing Science and Engineering Conference, vol. 85819, V002T05A035.

Gutiérrez, Ignacio Montes, et al., 2023. Neighbourhood models induced by the euclidean distance and the kullback-leibler divergence. In: Proceedings of Machine Learning Research.

He, Kaiming, Zhang, Xiangyu, Ren, Shaoqing, Sun, Jian, 2016. Deep residual learning for image recognition. In: Proceedings of the IEEE Conference on Computer Vision and Pattern Recognition. pp. 770–778.

Hsu, Chia-Yu, Liu, Wei-Chen, 2021. Multiple time-series convolutional neural network for fault detection and diagnosis and empirical study in semiconductor manufacturing. J. Intell. Manuf. 32 (3), 823–836.

Hu, Zhining, Schlosser, Tobias, Friedrich, Michael, Silva, Beuth, Frederik, Kowerko, Danny, 2024. Utilizing generative adversarial networks for image data augmentation and classification of semiconductor wafer dicing induced defects. In: 2024 IEEE 29th International Conference on Emerging Technologies and Factory Automation. ETFA, pp. 1–4.

Kang, SeungGu, Jeon, Sangmoo, Ryu, Kihwan, Shin, Joonghan, 2025. Online monitoring of weld cross-sectional shape using optical emission spectroscopy and neural network during laser dissimilar welding. Eng. Appl. Artif. Intell. 141, 109847.

Kim, Yusung, Cho, Donghee, Lee, Jee-Hyong, 2021. Wafer defect pattern classification with detecting out-of-distribution. Microelectron. Reliab. 122, 114157.

Li, Yanfeng, Gao, Xiangdong, Zheng, Qiaoqiao, Gao, Perry P., Zhang, Nanfeng, 2019. Weld cracks nondestructive testing based on magneto-optical imaging under alternating magnetic field excitation. Sensors Actuators A: Phys. 285, 289–299.

Li, Y.B., Wang, B., Shen, Q., Lou, M., Zhang, H., 2013. Shunting effect in resistance spot welding steels—part 2: theoretical analysis. Weld. J. 92 (8), 231s–238s.

Li, Y., Zhang, Y., Luo, Z., Shan, H., Feng, Y.Q., Ling, Z.X., 2016. Failure mode transition of triple-thin-sheet aluminum alloy resistance spot welds under tensile-shear loads. Weld J. 95, 479s–490s.

Liu, Chang, Antypenko, Ruslan, Sushko, Iryna, Zakharchenko, Oksana, 2022. Intrusion detection system after data augmentation schemes based on the VAE and CVAE. IEEE Trans. Reliab. 71 (2), 1000–1010.

MohammadiSefat, MohammadJavad, Ghazanfari, Hadi, Blais, Carl, 2021. Friction stir welding of 5052-H18 aluminum alloy: Modeling and process parameter optimization. J. Mater. Eng. Perform. 30, 1838–1850.

Nielsen, Chris Valentin, Friis, Kasper Storgaard, Zhang, W., Bay, Niels, 2011. Three-sheet spot welding of advanced high-strength steels. Weld. J. 90 (2), 32s–40s.

Pouranvari, M., Marashi, S.P.H., 2011. Critical sheet thickness for weld nugget growth during resistance spot welding of three-steel sheets. Sci. Technol. Weld. Join. 16 (2), 162–165.

Pouranvari, M., Marashi, S.P.H., 2012. Weld nugget formation and mechanical properties of three-sheet resistance spot welded low carbon steel. Can. Metall. Q. 51 (1), 105–110.

Shen, Jie, Zhang, Yansong, Lai, Xinmin, Wang, P.C., 2011. Modeling of resistance spot welding of multiple stacks of steel sheets. Mater. Des. 32 (2), 550–560.

Vo, Quoc-Trinh, Tran, Dat Van, Nguyen, Rin Vy, Le, Ngoc Anh, Truong, Cong Doan, Tran, Tin Trung, 2023. LSTM-based welding quality forecasting system in smart manufacturing. In: Proceedings of the 2023 9th International Conference on Robotics and Artificial Intelligence. pp. 54–60.

Wang, Bing, 2023. A study on spot welding quality judgment of stainless steel plate based on semi-supervised conditional generation adversarial network. Adv. Mech. Eng. 15 (2), 16878132231154138.

Xia, Yu-Jun, Lv, Tian-Le, Ghassemi-Armaki, Hassan, Li, Yong-Bing, Carlson, Blair E., 2023. Collaborative simulation of nugget growth and process signals for resistance spot welding. Weld. World 67 (6), 1377–1392.

Xia, Yu-Jun, Zhou, Lang, Shen, Yan, Wegner, Diana M., Haselhuhn, Amberlee S., Li, Yong-Bing, Carlson, Blair E., 2021. Online measurement of weld penetration in robotic resistance spot welding using electrode displacement signals. Measurement 168, 108397.

Xiao, Meng, Yang, Bo, Wang, Shilong, Zhang, Zhengping, He, Yan, 2023. Fine coordinate attention for surface defect detection. Eng. Appl. Artif. Intell. 123, 106368.

Yang, Bo, Zhang, Yang, Wang, Shilong, Xu, Weichun, Xiao, Meng, He, Yan, Mo, Fan, 2022. A global interactive attention-based lightweight denoising network for locating internal defects of CFRP laminates. Eng. Appl. Artif. Intell. 116, 105436.

Zhang, Yanxi, Gao, Xiangdong, You, Deyong, Zhang, Nanfeng, 2019a. Data-driven detection of laser welding defects based on real-time spectrometer signals. IEEE Sensors J. 19 (20), 9364–9373.

Zhang, Kai, Tang, Baoping, Qin, Yi, Deng, Lei, 2019b. Fault diagnosis of planetary gearbox using a novel semi-supervised method of multiple association layers networks. Mech. Syst. Signal Process. 131, 243–260.

Zhang, Ji, Wu, Xiao, Cheng, Zhi-Qi, He, Qi, Li, Wei, 2023. Improving anomaly segmentation with multi-granularity cross-domain alignment. In: Proceedings of the 31st ACM International Conference on Multimedia. pp. 8515–8524.

Zhou, Lei, Zheng, Wenjia, Li, Tianjian, Zhang, Tianyi, Zhang, Zhongdian, Zhang, Ye, Wu, Zhicheng, Lei, Zhenglong, Wu, Laijun, Zhu, Shiliang, 2020. A material stack-up combination identification method for resistance spot welding based on dynamic resistance. J. Manuf. Process. 56, 796–805.